ARTICLES
https://doi.org/10.1038/s41928-020-0391-2
nature electronics

Charge-programmed three-dimensional printing for multi-material electronic devices

Ryan Hensleigh[1,2,7], Huachen Cui[1,3,7], Zhenpeng Xu[1,3], Jeffrey Massman[4], Desheng Yao[1,3], John Berrigan[4] and Xiaoyu Zheng[1,2,3,5,6] ✉

Three-dimensional (3D) printing can create complex geometries that could be of use in the development of electronics. However, the approach is mainly limited to non-functional structural materials, and the 3D printing of electronic devices typically requires multiple process stages of embedding, spraying and writing. Here, we report a 3D printing approach that can volumetrically deposit multiple functional materials within arbitrary 3D layouts to create electronic devices in a single step. Our approach prints 3D structures with a programmable mosaic of distinct surface charge regions, creating a platform to deposit functional materials into complex architectures based on localized electrostatic attraction. The technique allows selective volumetric depositions of single metals and also diverse active material combinations, including ceramic, semiconducting, magnetic and colloidal materials, into site-specific 3D topologies. To illustrate the capabilities of our approach, we use it to fabricate devices with 3D electronic interfaces that can be used for tactile sensing, internal wave mapping and shape self-sensing.

Creating defined patterns is key to building functional devices such as integrated circuits, microelectromechanical systems (MEMS), antennas, sensors, actuators and metamaterials[1]. Microfabrication based on traditional lithography, deposition, etching and release is well suited to creating planar, two-dimensional (2D) patterned devices built from similarly flat substrates[1]. However, these 2D design processes are unsuited to the creation of isotropic[2,3], structural[4] or conformable 3D devices[5–7]. Complex, non-planar 3D substrates are not compatible with post-processing by traditional lithographic and extrusion/spray[8,9] methods due to shadowing/blockage of internal areas by the external substrate features (such as beams and walls) of the 3D structure[2,3]. Using lithography and then straining the substrate to deform planar patterns into 3D structures has been used to make functional 3D devices, but the approach is limited in resolution, complexity and periodicity[5–7].

Three-dimensional printing can, in principle, access any arbitrarily complex structure, but it is limited mostly to non-functional, structural materials due to the trade-off between ease of processing and functionality[10,11]. Each individual functional ink must be optimized for the chosen 3D printing technique, requiring significant development time for new materials. Current 3D-printed devices typically require multiprocess sequential writing techniques[4,12,13], combining multiple printing, infilling[14] and wire embedding[15] stages to form a functional device. The requirements for print pausing, switching between techniques and subsequent layer alignment during layer-by-layer techniques[16] lead to excessive build times and require extensive printing path optimization, limiting access to complex 3D electrode interfaces and geometries.

In this Article, we report a method to produce 3D devices by programmed volumetric deposition of one (or multiple) materials into arbitrary 3D micro-architectures. This is achieved by controlling the electrostatic charges and consequent absorptive properties of our optically 3D patterned feedstock material. This creates a 3D charge-programmed mosaic from which a variety of materials can be deposited at pre-defined locations within the structure. The method eliminates the need for multiprocess printing[13], allows flexibility of design, does not require complex conjugation chemistries[17] and eliminates the need to develop new printer feedstocks for each material. With this approach, we demonstrate microscale selective depositions of several materials, including metallic, ceramic, semiconducting and magnetic materials, either singularly or in combination with multiple depositions. Our technique, combined with multifunctional materials, allows the one-step fabrication of smart materials and transducers with 3D embedded electrodes. We use our approach to create devices capable of 3D tactile mapping, internal wave mapping and 3D capacitance shape sensing.

Programming deposition in three dimensions

Our 3D selective deposition scheme is based on controlling the surface charge between 3D-printed substrate materials and the materials to be deposited. To achieve this, we prepare a charge-programmable pallet by varying the pendant reactive groups present in the pre-polymer monomer. These reactive groups can be classified as positive (such as ammonium and phosphonium), negative (such as phosphate and carboxylate) or neutral (such as ethylene and ether groups) (Fig. 1a) and, when combined with photo-crosslinkers, form a 3D patternable resin, which, after optical patterning, maintains the distinct charge polarity of its parent material. Through a custom multi-material projection micro-stereolithography system (Supplementary Fig. 1) with fluid switching, the arrangement of each charged region's distributions is patterned into a 3D architecture, programmed by the part's digital design. This electrostatic mosaic, combining positive, negative and neutral areas, forms a patterned substrate upon which microfabrication can be carried out. By exploiting the charge difference between each sub-domain, our programmable 3D deposition platform emerges based on simple

[1]Department of Civil and Environmental Engineering, University of California Los Angeles, Los Angeles, CA, USA. [2]Macromolecules Innovation Institute, Virginia Tech, Blacksburg, VA, USA. [3]Department of Mechanical Engineering, Virginia Tech, Blacksburg, VA, USA. [4]Materials and Manufacturing Directorate, Air Force Research Laboratory, Wright Patterson Air Force Base, OH, USA. [5]Department of Mechanical and Aerospace Engineering, University of California Los Angeles, Los Angeles, CA, USA. [6]California NanoSystems Institute, University of California, Los Angeles, Los Angeles, CA, USA. [7]These authors contributed equally: Ryan Hensleigh, Huachen Cui. ✉e-mail: rayne@seas.ucla.edu

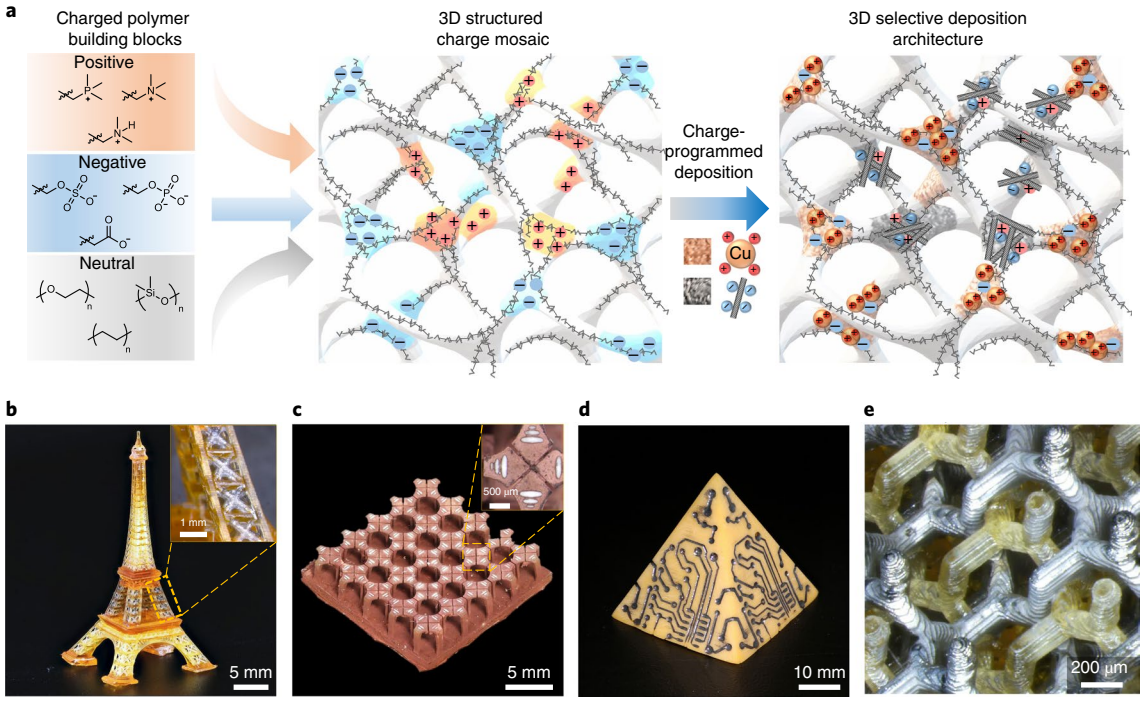

Fig. 1 | Programmable deposition in three dimensions. a, Schematic for programmed electrostatic charge deposition of materials in 3D. The deposition is rapid (26,000 $mm^2 h^{-1}$), which is nearly five times faster than the next most rapid similar technique, at 5,600 $mm^2 h^{-1}$ (aerosol jet printing). **b**–**e**, Structures can be arbitrarily complex: the Eiffel Tower, with the internal struts of the main beams in the middle section plated with metallic-grey Ni–P (**b**); a 3D antenna array with white dielectric and red copper areas (**c**); a circuit on an arbitrary 3D pyramid substrate (**d**); an interpenetrating metal–dielectric double gyroid (**e**).

rules: when the sub-domain and deposition material have opposite charge polarity, there is attraction and deposition; and like polarity or no polarity (neutral) repels or gives no significant plating.

To demonstrate our scheme, we formulated blends of charged acrylic monomers and neutral crosslinkers, a radical initiator and dye to form photo-sensitive charged resins that can be shaped into complex 3D architectures (see Methods). We sculpted positive, negative and neutral resins into a variety of 3D structures, which were soaked in either a positive or negative Pd salt solution and subsequently placed in electroless nickel-phosphorus (Ni–P) or copper (Cu) solution to deposit metal into the oppositely charged areas of the structures. In this way, structures such as a microscale Eiffel Tower, antenna arrays or interpenetrating double gyroids could be formed (Figure 1b–e). Supplementary Video 1 demonstrates the process of patterning a topological 3D circuit, which is completed within a few minutes.

The Pd triggers an autocatalytic metal deposition process. For example, in the metallic-grey Ni–P plating, Pd oxidizes native hypophosphite ions $\left(H_2PO_2^-\right)$ (equation (1)) to trigger nickel metal (Ni^0) (equation (2)) and phosphorus (P) (equations (3) and (4)) reduction and co-deposition (the Cu plating process is described in Supplementary Note 1)[18,19]:

$$H_2PO_2^- \rightarrow H^{\bullet} + HP^{\bullet}O_2^- \quad (1)$$

$$Ni^{2+} + 2H^{\bullet} \rightarrow Ni^0 + 2H^+ \quad (2)$$

$$H_2PO_2^- + H^{\bullet} \rightarrow H_3PO_2 \quad (3)$$

$$H_3PO_2 + H^{\bullet} \rightarrow P + 2H_2O \quad (4)$$

The key requirement is the selective adsorption of the Pd catalyst to localize deposition to our pre-programmed areas. Through scanning electron microscopy–energy dispersive X-ray spectroscopy (SEM-EDX), we observe that the charged Pd catalysts are highly selective for their oppositely charged counterparts after soaking for only a few minutes, but they show no detectable adsorption to uncharged or like-charged substrates, even after hours (Supplementary Figs. 2 and 3), confirming our selective deposition process. This selectivity holds until reaching the current repeatable feature size limit of our multi-material 3D printing technique at ~10 µm (Supplementary Fig. 4). Our selective metallic features are highly conductive and can be combined with Cu electroplating to produce metallic features with high conductivity (1.2×10^7 S m^{-1}), approaching the value for bulk Cu (5.96×10^7 S m^{-1}; ref. [20]), making them ideal for electronic applications (Supplementary Fig. 5).

Comparing the speed and resolution of our method to other methods for 3D printing of electrical devices (Supplementary Table 1), such as sequentially extruded ink[8,21] or liquid metal[22] (0.2–113 $mm^2 h^{-1}$, 10–120 µm), aerosol jet[23] (19–5,600 $mm^2 h^{-1}$, 100 µm) and multiprocess techniques[13] (11 $mm^2 h^{-1}$, 100 µm), our selective volumetric deposition method allows programmed metallic contacts to form rapidly (26,000 $mm^2 h^{-1}$, 10 µm), with internal features and complex structures that are unmatched by these processes. The ability to deposit metals in essentially any area (internal or external) of a 3D structure through a rapid 3D printing approach opens new opportunities to rapidly manufacture, ad hoc, many conductor/dielectric devices, including electrodes, antennas and sensors. Importantly, our techniques are not limited to stereolithography. The wide variety of commercially available charged polymers and the simplicity of our techniques open the possibility of integrating our methods with essentially any 3D printing technique.

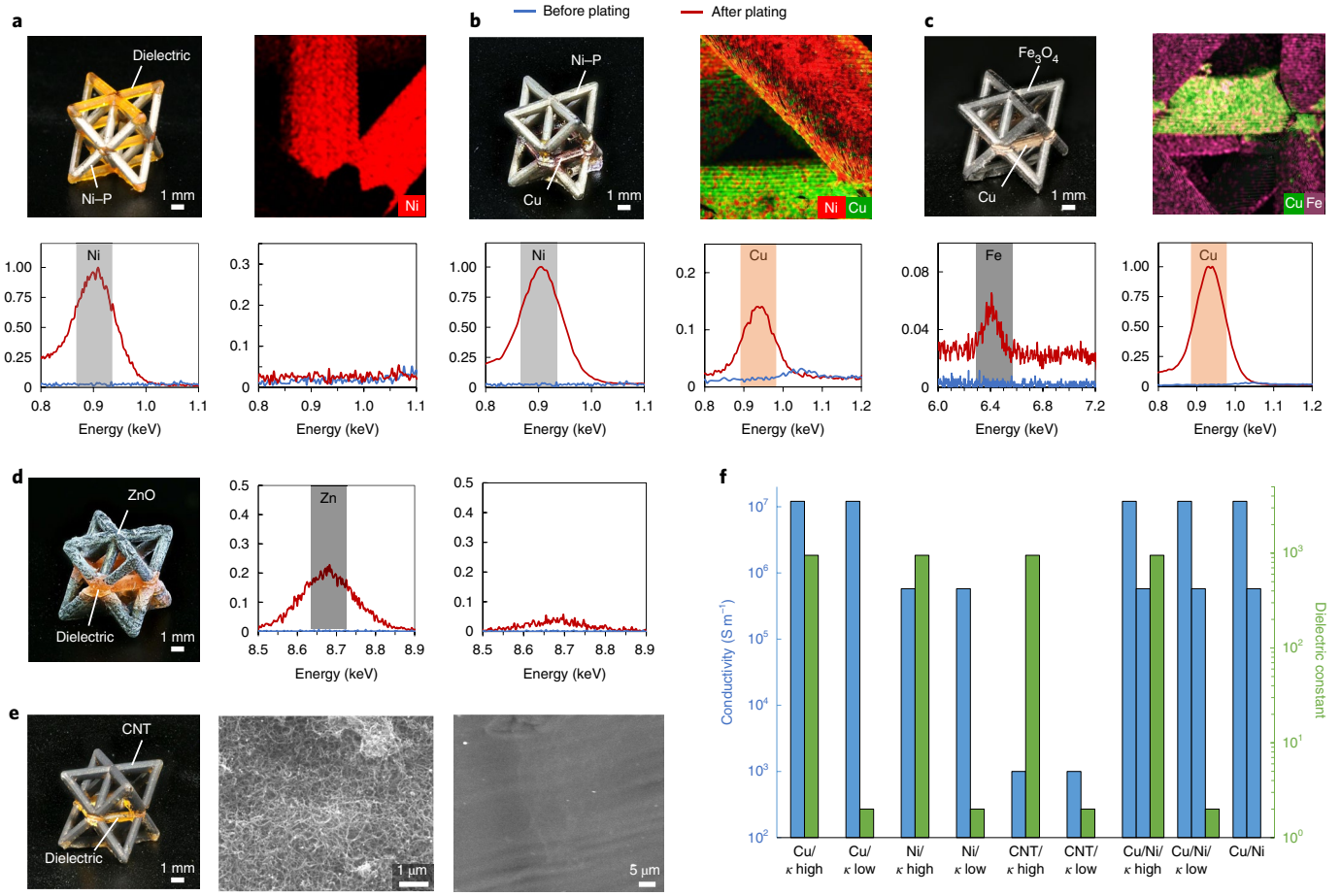

Fig. 2 | Multi-material deposition. a, Selective nickel octet: SEM-EDX mapping (top) and graphs (bottom) showing the elemental composition of each respective area. **b**, Bimetallic octet truss with Cu and Ni beams. SEM-EDX mapping (top) and graphs (bottom) confirm Cu and Ni deposition. **c**, Composite octet truss combining Cu and ceramic magnetite (Fe_3O_4). SEM-EDX mapping (top) and graphs (bottom) confirm Cu and Fe deposition. **d**, Plated semiconductor ZnO and dielectric polymer with SEM-EDX mapping (left) and graphs (right). **e**, Selectively plated carbon nanotubes dispersed with charged surfactant (left). SEM images show the nanotubes network present in dark coloured areas and polymer areas with no nanotube deposition. **f**, A variety of conductivity/dielectric combinations showing the wide range of properties we can achieve.

Selective multi-material volumetric depositions

Using a 3D unit cell digital model, we demonstrate programmed selective 3D patterning for a variety of materials, from single-material to multi-material selective co-depositions (Fig. 2a). As shown in Supplementary Videos 2 and 3, programmed plating of Ni–P occurs at selectively activated sub-domains within a 3D micro-architecture. SEM-EDX mapping of the cell strut junctions confirms the presence of Ni in the designed locations, and SEM-EDX spectra show no detectable contamination outside these areas (Fig. 2a).

Our techniques are not limited to Ni–P and Cu metal/dielectric combinations; magnetic[24], ceramic[25] and semiconductor[26] dielectric combinations are amenable to our techniques through established electroless methods. Additionally, the high selectivity of Pd catalyst for only its oppositely charged sub-domain as well as its inert response to previously plated materials allow us to plate multiple materials through successive deposition schemes, creating further combinations of dielectric/conductor/magnetic/semiconductor and so on. Our scheme is illustrated in Supplementary Fig. 6. For example, an as-fabricated bimetallic Cu and Ni–P octet-truss unit cell is shown in Fig. 2b. To fabricate this, we begin with an initial structure consisting of positively charged horizontal, square core beams, with the remaining structure being negatively charged. Soaking in negatively charged Pd solution catalyses only the positive areas, which are subsequently plated with Cu in an electroless bath. Once finished, the part is placed in a positive Pd solution, catalysing only the negative, unplated areas. Placing the structure in a Ni–P bath plates the remaining uncoated beams of negative resin with metallic-grey Ni–P. The Cu surface is unreactive to the Pd catalyst and the Ni–P plating under our chosen conditions[27]. SEM-EDX results confirm the presence of Cu and Ni at the expected 0.928 keV and 0.849 keV peaks, respectively, with no detected cross-contamination[28].

This material flexibility opens many interesting opportunities for exploring 3D electromagnetic, semiconductor and other devices. In Fig. 2c, we demonstrate a metal–metal oxide composite octet truss, with one phase being copper and the other (black) magnetite (Fe_3O_4) (ref. [24]). SEM-EDX confirmed the presence of each material, with iron (Fe) having the expected 6.5 keV peak and crystalline structure by X-ray diffraction (XRD in Supplementary Fig. 7)[28] and no detected cross-contamination (Supplementary Fig. 8). Wide-bandgap, n-type semiconducting zinc oxide (ZnO) was plated and combined with a dielectric polymer (Fig. 2d) and also confirmed by SEM-EDX, with Zn detected at the expected 1.0 keV peak and with a wurtzite crystal structure in XRD (Supplementary Fig. 9)[26,28]. Combining the high electrical conductivity of our Cu deposits with the ferrimagnetic properties of magnetite, or the semiconducting properties of ZnO and a dielectric, open new opportunities for 3D mesoscale electromagnetic and semiconducting metamaterials through our manufacturing process.

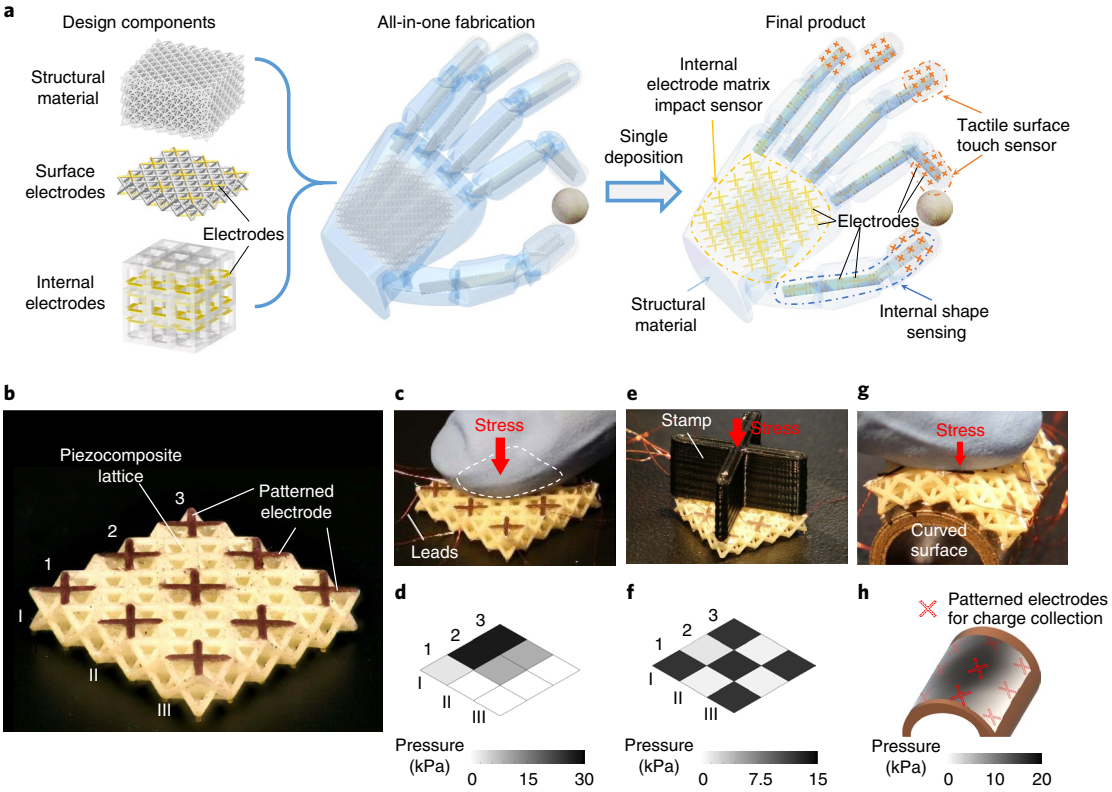

Fig. 3 | Tactile mapping by selective electrode pixels. a, Schematic of an all-in-one embedded smart self-sensing device that can be fabricated using our methods. **b**, The as-fabricated tactile sensor and electrode numbering. **c**,**d**, Optical image of the conformal tactile sensor while applying pressure with the fingertip (**c**) and the corresponding pressure map (**d**). **e**,**f**, Optical image of the conformal tactile sensor while applying pressure with a stamp (**e**) and the corresponding pressure map (**f**). **g**,**h**, Optical image of the conformal tactile sensor on a curved surface while applying pressure with a fingertip (**g**) and the corresponding pressure map (**h**).

Our techniques can be extended to program 3D patterning of colloidal materials including carbon nanotubes (Fig. 2e). This is achieved by simply soaking our charged substrates in a solution of the nanomaterial dispersed with commonly used charged surfactants such as negatively charged sodium dodecyl sulfate (SDS). SDS creates a negative CNT dispersion[29], which allows rapid deposition to an oppositely charged positive substrate. SEM confirmed the presence of conductive (1,000 S m^{-1}) nanotube networks in the oppositely charged areas, while polymer areas remained free of deposits. The wide variety of nanomaterials that can be dispersed with charged surfactants creates a nearly endless palette for material deposition and device development.

The dielectric properties of the incorporated polymer may also be individually tuned across two orders of magnitude, from the ultra-low range (~1–3) to the ultra-high (>800) by incorporation of dielectric ceramic nanoparticles (Supplementary Fig. 10)[11]. Our technique thus allows access to a wide range of dielectric/conductive patterning in 3D arbitrary micro-architectures; some of these are summarized in Fig. 2f. A key to functional devices is the combination of multiple materials within distinct areas[1]. The wide variety of available materials (including metal, magnetic, ceramic, semiconducting and nanomaterial) paired with the tunable dielectric properties of our polymer creates a complex and nearly endless palette with which to build functional 3D devices. In the following, we exploit a variety of unique applications that combine responsive materials with internally printed electrode arrays.

Tactile sensor with patterned electrodes

An intriguing application of our technique is the fabrication of a smart prosthesis and sensor in one integrated step, with customizable free form factors and individually addressable 3D electronic interfaces, not achievable in current approaches[30–33]. Our method seamlessly combines structural and functional materials to provide human-like responses, including tactile, impact and 3D shape-sensing aspects (Fig. 3a). We first demonstrate a proof of concept by conformally patterning copper electrodes onto a flexible piezoelectric active composite foam, producing a tactile pressure transducer in one simple step.

We first synthesized highly responsive piezoelectric nanocomposites by surface-treating lead-zirconate-titanate (PZT) nanoparticles with silane acrylates. The functionalized PZT particles were combined with neutrally charged photo-sensitive monomers at high volume fractions (10 vol%) and multi-materially printed with charged resins to form the complex structure[11]. The charged resin formed nine individual electrode pairs (coated with Cu), which collect site-specific electric charges from the piezoelectric neutral resin when the structure is deformed. The electrodes were patterned at programmed locations based on a 3D digital design for signal acquisition (Fig. 3b). The as-fabricated piezoelectric lattice was then activated via the corona poling method, converting pressure into electric charge via the calibrated piezoelectric charge constant g_{33} (see Methods), collected by the patterned electrode pairs. In this arrangement, each pair of electrodes acts as a pressure-detecting pixel for the piezoelectrics, which is connected to a resistor (10 MΩ) to form a closed circuit. The resistors are connected in parallel to a data acquisition system (DAQ) to read out the pressure-induced voltage. The voltages at each sites are collected by the DAQ and transferred to pressure using the measured g_{33} constant. Figure 3c–f shows the stress distributions measured on the 3×3 tactile sensor array while applying pressure with a fingertip (Fig. 3c,d) and a

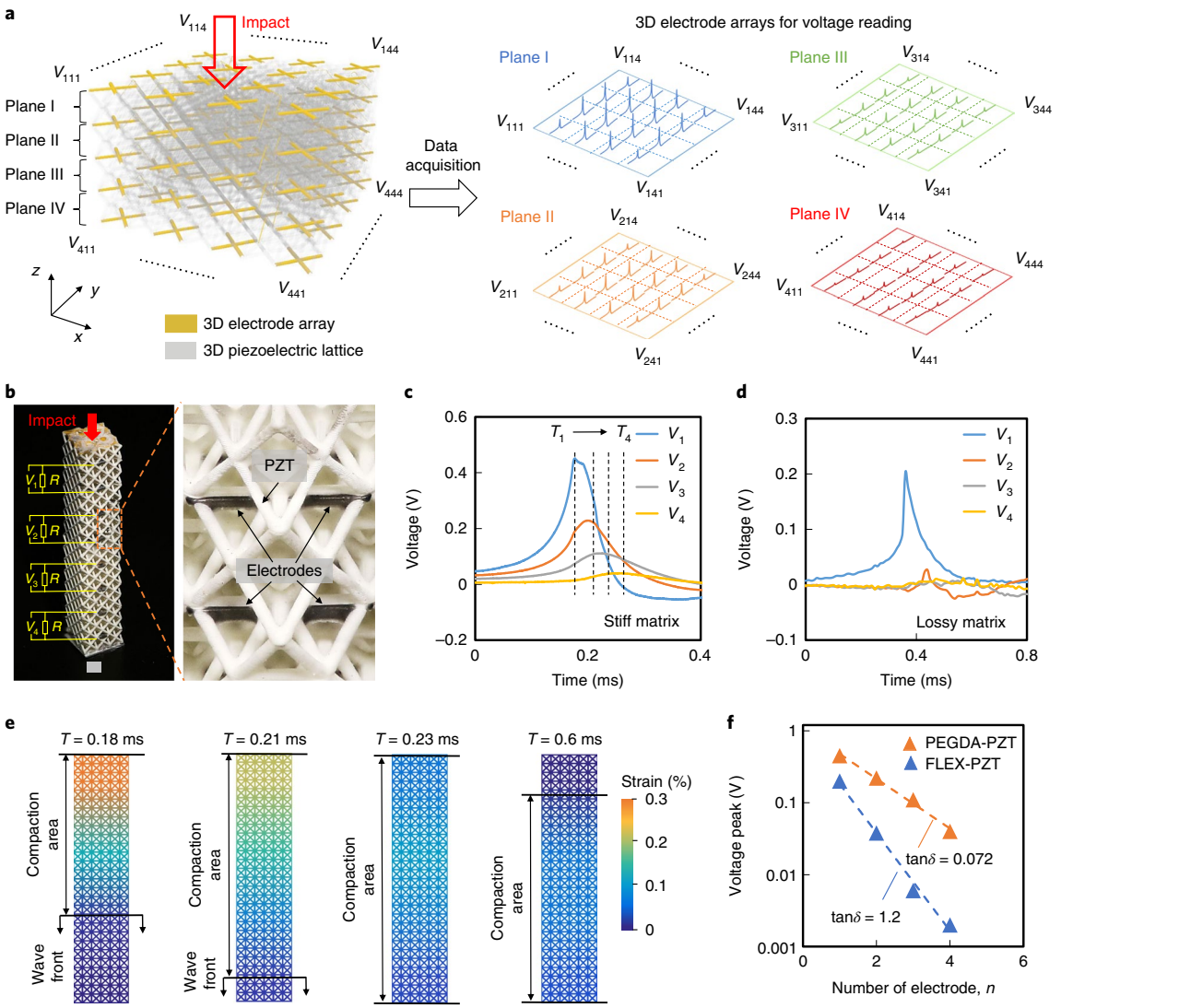

Fig. 4 | 3D strain sensor obtained by means of selective electrode deposition. a, Structure design, with internal electrodes for impact sensing. With a vertical impact, each horizontal plane of the structure is monitored for stress via an output voltage to reconstruct strain propagation. **b**, An as-fabricated piezoelectric lattice with selectively coated internal electrodes. **c**, Voltage outputs on different planes of the stiff PEGDA-PZT lattice as a function of time. **d**, Voltage output on different planes of the flexible FLEX-PZT lattice. **e**, Reconstructed strain profiles of the piezoelectric lattice at various time points, generated from the voltage output of the different planes in the stiff PEGDA-PZT lattice. The double-headed arrow shows the position of the elastic wavefront followed by a compaction area in the lattice (defined as where the strain becomes larger than 0.05%). **f**, Graph of voltage outputs from each plane of electrodes for both stiff (orange) and flexible (blue) lattices, where the slope corresponds to the damping of the structure.

stamp (Fig. 3e,f). The greyscale denotes the pressure level on various sensing cells of the tactile sensor; it can be seen that the position of the fingertip has been transferred successfully to the corresponding greyscale plots. We also show that a conformal tactile sensor can be readily achieved, providing pressure data for site-specific locations via patterned electrodes (Fig. 3g,h). Such a tactile sensor can act as the fingertip of a smart prosthesis, acquiring the fine detail of letters, surface roughness and complex shapes.

Impact wave mapping via embedded 3D electrode interfaces

A critical feature of natural human tissue (and thus for smart prostheses of the future) is its ability to detect impact and damage. This is a complex task, typically requiring external monitoring. Here, by volumetrically depositing addressable, 3D internal electrodes within any arbitrary 3D configuration, new opportunities for in situ monitoring of impact dynamics, with high throughput and spatially resolved sensing data acquisition, are possible within any complex architecture (Fig. 4a). This is not achievable with current methods. Here, by combining functionalized piezoelectrics with selective deposition of embedded electrodes, we demonstrate time- and spatially resolved internal stress and elastic wave mapping throughout a complex 3D structure.

To demonstrate the internal stress-sensing capabilities, we prepared composite lattice materials with different damping coefficients and detected elastic wave propagation within the architectures using volumetrically deposited electrodes. We 3D-printed piezoelectric nanocomposite lattices with different matrix materials, poly(ethyleneglycol) diacrylate (PEGDA) (high stiffness) and a urethane acrylate blend referred to as FLEX, a viscoelastic constituent material. Each as-fabricated lattice, stiff/PEGDA and flexible/FLEX, incorporated eight equidistant planes which were subsequently

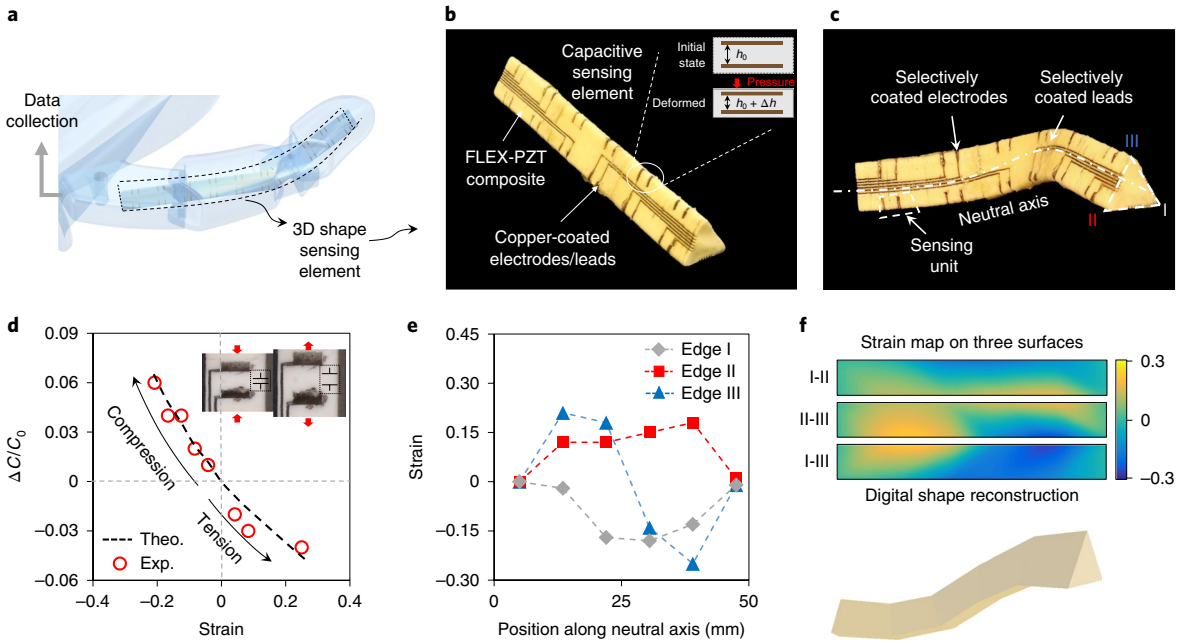

Fig. 5 | 3D shape sensor obtained by means of selective electrode deposition. a, Schematic of an all-in-one shape-sensing element. **b**, Optical image of the shape sensor with embedded electrodes on multiple planes and the capacitance-based sensing mechanism (inset). **c**, Optical image of 3D deformation of the shape sensor. **d**, Capacitance (*C*) change ratio under various strain conditions ranging from −0.2 to 0.3. **e**, Strain conditions of the shape sensor along the neutral axis. The red, blue and grey dashed lines mark the positions of the embedded electrodes. The strains are calculated from the relationship between the capacitance change ratio and the strain value, as shown in **c**. The middle point of each pair of electrodes determines the position of the corresponding electrodes. **f**, Strain maps and subsequent shape reconstruction based on the deformation in **d**.

deposited with copper to act as electrodes for monitoring the internal dynamic stress, as shown in Fig. 4b. The electrodes were each connected to resistors *R*, forming four independent, closed circuits. The resistors were connected in parallel to four channels of the DAQ (NI USB-6356) to read out the stress-induced voltage at both ends of the resistor. A 12 g steel ball was then dropped from 10 cm height onto the as-fabricated 3D piezoelectric lattice (attached to a rigid substrate; Supplementary Video 4). Propagation of the impact stress activated electric displacement of the piezoelectric metamaterial in the vertical direction, as shown in the traces of voltage output against time in Fig. 4c,d. The voltage outputs from the electrode pairs at each plane sequentially peak with time intervals that represent the propagation of the wave through the whole lattice.

The voltage output between each pair of electrodes traces the transient stress within the piezoelectric material (see Methods) triggered by the dropping impact. We reconstructed the strain maps of both lattices at various time points based on the voltage output (see Fig. 4e for the lattice with a stiff matrix and Supplementary Fig. 11 for the lattice with a lossy matrix), revealing the elastic wavefront propagation (defined as the junction between the elastically compressed and uncompressed regions of the lattice).

The internally deposited electrodes provide time- and spatially resolved wave mapping within 3D piezo-active smart materials at arbitrary locations. As the wavefront propagates through the structure, the peak strain (measured as voltage readings from electrodes patterned within each designed location, V_1, V_2, V_3, V_4) moves away from the top impact layer, with decreasing amplitude at each sequential layer (Fig. 4c–e), indicating how the piezoelectric lattice materials absorb and damp out the energy generated from the drop impact. Figure 4f plots the measured voltage peaks (V^p) as a function of each distributed electrode layer within the different lattice materials used. The voltage readings from patterned electrodes at each internal layer allow us to visualize and extract the damping coefficients within the lattice material through which the excited elastic wave propagates. The slopes of the fitted curves in Fig. 4f reveal the effective loss factor, tanδ, of the metamaterial:

$$\tan\delta = \sqrt{\frac{\beta^2(1-r^2)^2-1}{r^2(1-\beta^2)}} \quad (5)$$

where β is the slope of the curves in Fig. 4f, namely $\log\left(\frac{V_n}{V_{n-1}}\right)$. The logarithm of the measured voltage shows an approximately straight-line relationship with the depth of the lattice moving away from the impact (represented by electrode location number n). The different slopes reveal the different effective loss factors of the intrinsic materials (calculated from the slope as 0.078 for the PEGDA-PZT composite lattice and 1.2 for the FLEX-PZT composite lattice). The measured effective loss factor closely matches direct testing results obtained by dynamic mechanical analysis (TA Instrument DMA 850), as shown in Supplementary Table 2, supporting the high fidelity of our method.

Shape self-sensing and reconstruction

To fabricate prosthetics and soft robots, the incorporation of conductive electrodes can facilitate self-sensing and proprioception functions, which are critical to allow more advanced arbitrary movements to occur in these systems[33]. As a proof-of-concept demonstration, a flexible 3D shape-sensing device (Fig. 5a–c) based on an array of capacitive sensors was printed and coated to form embedded metal electrodes.

This structure is a simplified arm consisting of FLEX polymer and 8 vol% unfunctionalized PZT particles (to form a high-dielectric-constant (~156) composite). Figure 5b presents an optical image of the all-in-one fabricated shape-sensing device. The as-fabricated device contains 36 internal electrodes, forming 18 capacitive sensors located on three edges of the device for deformation detection of the corresponding sections (see Methods). The capacitive sensor

arrays are individually connected to commercial capacitance meters (KNACRO LC100-A) to capture the capacitance change. Figure 5d shows the capacitance change ratio ($\Delta C/C_0$) as a function of strain for an individual capacitive sensor. The performance of the capacitive sensor was characterized by stretching or compressing the device along the longitudinal direction. With stretch or compression, the sensor expands or shrinks, resulting in a localized capacitance change between each of the capacitive sensors. The device flexing and strain were tested in a range of ~−0.2–0.3. Figure 5c shows an example deformation of the shape-sensing device. As the device deforms, a capacitance meter monitors the deformation, which is translated to the strain between each two corresponding electrodes. Figure 5e plots the strain versus longitudinal position corresponding to the centre point of the sensors on three edges of the device. Using cubic spline interpolation of the strain, a strain map of the shape-mapping area was generated and the shape of the element was reconstructed; this matches the real case well, as shown in Fig. 5f. This 3D-printed device proves the possibility of integrating sensors and the underlying structural material in an all-in-one process. The ability of a device to sense its own shape is a significant step towards ad hoc prosthetic and soft-robotic fabrication with integrated sensing.

Conclusions

We have reported a device fabrication scheme based on selective volumetric deposition of materials within a complex 3D structure. Our charged mosaic projection microlithographic approach can be used to create functional devices through localized deposition of single or multiple diverse materials within an arbitrarily complex architecture. This is in contrast with typical printing and integration approaches, which involve multiple steps, alignment and embedding. We demonstrate the capabilities of the approach by using it to fabricate a 3D-printed device with tactile, impact and shape-sensing features in one integrated manufacturing process. This technique could be used to develop advanced prosthetics, metamaterials, antennas and soft robotics with integrated functionality and 3D electrode interfaces.

Our approach is not limited to optical patterning: charged inks that are compatible with other writing process could be used to achieve the desired volumetric deposition of electrode arrays. Tuning crosslinker functionality and backbone structures would allow the use of polymers with tunable mechanical stiffness, including urethanes and siloxanes (kPa), high-stiffness multiacrylates (GPa) and acrylate-derived high-temperature polymers. Beyond varying the polymer chemistry, our process allows the use of polymer composites with a wide range of thermal, electrical, ionic and optical material properties, making our techniques amenable to diverse functional applications. Furthermore, the technique can employ widely available materials and access a variety of sophisticated plating schemes. The process of programmed deposition in 3D opens new opportunities to combine 3D topologies with electronic microfabrication techniques so as to build 3D functional devices.

Methods

Materials. Most resin materials, catalysts, zinc oxide (ZnO) and magnetite (Fe_3O_4) deposition materials were purchased from Sigma-Aldrich and used as received: bis(2-(methacryloyloxy)ethyl))phosphate (PDD), (2-(acryloyloxy)ethyl) trimethylammonium chloride solution 80 wt% in H_2O (TMAA), bisphenol A glycerolate dimethacrylate (BisGMA), trimethylpropane triacrylate (TMPTA), polyethylene glycol diacrylate M_n ~250 (PEGDA), 1,6-hexanediol diacrylate (HDDA), phenylbis(2,4,6-trimethylbenzoyl)phosphine oxide (Irg819), Sudan(I), sodium tetrachloropalladate(II) (Pd−), tetraaminepalladium(II) chloride monohydrate (Pd+), iron(III) nitrate nonahydrate, zinc nitrate hexahydrate, borane dimethylamine complex (DMAB), sodium dodecyl sulfate (SDS), 3-(trimethoxysilyl)propyl methacrylate (TMSPM), glacial acetic acid, hydrochloric acid and reagent-grade sodium chloride (NaCl). For the flexible (FLEX) resins, Ebecryl 242 and 114 were donated by Allnex. Multi-walled CNTs (MWCNTs, 20–30 nm outer diameter) were purchased from Cheaptubes. Piezoelectric nanoparticle PZT (APC850 and APC855) was purchased from APC International.

Electroless metal plating solutions were purchased from Caswell and used as received (Electroless Copper Kit and Electroless Nickel). For the Caswell provided catalysts, the 'sensitizer' and 'activator' solutions were not used.

Resin formulations. *Negative resin (50%).* Negative resin (50%) composed of 5 g PDD, 5 g TMPTA, 0.2 g Irg819 and 0.015 g Sudan(I) was used for the majority of the paper.

Positive resin. The positive resin was composed of 5 g TMAA, 5 g BisGMA, 0.2 g Irg819 and 0.015 g Sudan(I) was used.

Neutral (TMPTA) resin. The neutral (TMPTA) resin was composed of 10 g TMPTA, 0.2 g Irg819 and 0.015 g Sudan(I).

Neutral (PEGDA) resin. The neutral (PEGDA) resing was composed of 10 g PEGDA, 0.2 g Irg819 and 0.015 g Sudan(I).

Neutral (HDDA) resin. The neutral (HDDA) resin was composed of 10 g HDDA, 0.2 g Irg819 and 0.015 g Sudan(I).

Piezoelectric resins. For piezoelectric resins and resins of varying dielectric constant, various amounts of PZT from 1 to 40 vol% were combined with PEGDA and then dispersed with a high-energy ball mill (Retsch) for 30 min (based on our previous work[11,34]). The wave-mapping demo used a 3 vol% functionalized PZT-PEGDA resin. To functionalize PZT, 0.5 g PZT, 1.049 g TMSPM and 1.049 g glacial acetic acid were added to 50 g of deionized (DI) water, followed by sonication for 15 min, then refluxing while stirring for at least 4 h. After washing twice with water and once with ethanol, it was then dried before dispersing using a high-energy ball mill. The shape-sensing resin consisted of 20 vol% of unfunctionalized PZT in PEGDA with 2 wt% Irg819 (to polymer). The FLEX resin consisted of 3.4 g of Ebecryl 114 in 6.6 g Ebecryl 242 with 0.2 g Irg819 and 0.015 g Sudan (I).

Charged solutions. Pd+ solution. Tetra-amine palladium chloride (0.0562 g) was added to 20 g DI water (this solution should be used the same day it is made).

Pd− solution. Sodium tetrachloropalladate (0.0588 g) in 20 g pH 4.88 solution (using HCl), 0.21 g NaCl, was used, based on ref. [35]. The solution seemed stable for multiple days, but was typically used the same day it was made.

Electroless Ni–P. As per the Caswell instructions, 1 part A, 3 parts B and 16 parts DI water were combined and used as is. The solution seemed stable for at least one week.

Electroless Cu. As per the Caswell instructions, 1 part A and 1 part B were combined and used as is. The solution should be used the same day as it is made.

Fe_3O_4 deposition solution. Based on the work of Nakanishi and others[24], 0.0177 g (0.03 M) DMAB and 0.0101 g (0.0025 M) iron(III) nitrate nonahydrate were added to 10 g DI water. The solution should be used the same day as it is made.

ZnO deposition solution. Based on the work of Saito and others[26], 0.2975 g (0.05 M) zinc nitrate hexahydrate and 0.0118 g (0.01 M) DMAB were added to 20 g of DI water. The solution seemed stable for at least a week, but was used the same day as it was made.

CNT deposition. MWCNTs (0.01 g) and 0.02 g SDS were added to 10 g DI water and sonicated. The black supernatant was used as is.

Multi-material 3D printing. To manufacture our structures we utilized a custom-made bottom-up, multiple-vat projection stereolithography system[36]. Blends of each charged monomer and neutral crosslinkers (called resin) were contained separately in a bath chamber with a transparent siloxane membrane bottom. The baths were located on a mobile platform so that they could be arbitrarily aligned between the build substrate and a dynamic photomask. The build substrate, dipping into each bath to a fixed height, was exposed to a defined 2D light pattern, solidifying the liquid resin into a single layer bound to the build substrate forming the first sub-domain of the structure. The substrate and structure were removed from the resin, cleaned using an ethanol rinse, dried under flowing air, dipped into a secondary (or tertiary, quaternary and so on) resin, and exposed to another 2D light pattern to build a layer of the material to form another sub-domain of the same 3D part. The process was repeated layer by layer, combining the multiple materials into a 3D structure.[36]

Selective deposition. Caswell solutions were used as received. The provided 'activator' and 'sensitizer' solutions were not used. Parts were dipped into their respective catalyst (Pd+ or Pd−) solutions for 1–30 min. Sonication or a pipette were sometimes used to remove air bubbles in complex parts. The part was removed with tweezers and wick-dried with a Kimwipe. Complex parts, or parts with fine features,

were then blown with air for a short time to remove trapped catalyst (which can accumulate in small crevices and cause plating in areas where it should not occur). Parts could also be given a short DI wash for 5 s and then wick-dried again, but this can reduce the plating effectiveness. For multi-material depositions, the catalyst and plating process were repeated twice. If the plating features are on a part surface, one should take care not to excessively rub those areas when drying. Once catalysed, one of the following methods was used to deposit the material.

Ni–P and Cu deposition. Ni–P was plated at 80 °C and Cu at room temperature. The Ni–P process could take from 30 s to 10 min, depending on catalyst loading and temperature, to plate to a metallic-grey state. The Cu process with positive resin could take 0.5–2 h to give high-quality layers, while negative resin could take 10 min to several hours depending on catalyst loading.

Fe_3O_4 deposition. Magnetite was deposited at 80 °C and would typically deposit within 30 s to 5 min.

ZnO deposition. ZnO was deposited at 60 °C and would take 0.5–2 h to deposit a visibly noticeable layer.

MWCNT deposition. MWCNTs were deposited at room temperature by simply dipping into solution, waiting several minutes, removing, gently rinsing with water and drying.

Cu electrodeposition and measurement. A Caswell copper electrodeposition kit was used as received and according to their instructions. Electrodeposition required 1–10 min to achieve high conductivity in small parts. Plated features, such as the individual struts in Fig. 2, were removed by fracturing the structures, and their conductivity was measured using the four-point probe technique with a VersaSTAT3 instrument from Ametek. The conductivity was calculated according to

$$\sigma_{\text{film}} = \frac{\ln 2}{\pi t}\left(\frac{I}{V}\right)$$

where t is the thickness of the thin film. We fractured the struts and measured the thickness under a scanning electron microscope (EI Quanta 600 FEG), averaging the thickness measurements.

Dielectric measurement. The dielectric areas consisted of either pure photopolymer (PEGDA) or a composite of PEGDA, PZT powder varying from 0 to 40 vol% and initiator mixed by high-energy ball milling. To measure the dielectric constant of these composites, 7 mm × 7 mm × 0.08 mm solid films were printed and electrodes were deposited on the top and bottom surfaces to form a capacitor. The capacitance (C) of these films was measured on a commercial capacitance meter (KEYSIGHT E4990A) and the dielectric constants (ε_r) were calculated by

$$\varepsilon_{\text{r}} = \frac{Cd}{A\varepsilon_0}$$

where d is the distance between the electrodes (0.08 mm), A is the cross-sectional area of the samples (1 cm^2) and ε_0 is the electric constant (8.854×10^{-12} F m^{-1}). The dielectric constant could be varied over a wide range by varying the amount of dielectric powder within the photocurable polymer.

3D addressable electrode integration with piezo-active materials. The relationship between the pressure applied on the lattice (σ_t) and the voltage output induced by the pressure (V) is characterized as

$$\sigma_t = \frac{V(R_{\text{i}} + R)}{g_{33} dR} \tag{6}$$

where g_{33} is the piezoelectric voltage constant of the piezocomposite lattice, d is the distance between the adjacent electrodes and R_i is the internal resistance. The sensor was then pressed using a fingertip at various locations, as shown in Fig. 3. The nine sensing pixels generate voltages in response to the applied stress, which are collected by the DAQ.

Based on equation (6), the relationship between the strain (ε) of the lattice shown in Fig. 4 and voltage output (V) is

$$\varepsilon = \frac{V(R_{\text{i}} + R)}{g_{33} E_{\text{eff}} dR} \tag{7}$$

where E_{eff} is the effective modulus of the lattice. The constituent relationship can be described as[37]

$$m\ddot{\varepsilon}_n + \tan\delta\sqrt{\frac{E_{\text{eff}} Am}{L}}(\dot{\varepsilon}_n - \dot{\varepsilon}_{n-1}) + \frac{E_{\text{eff}} A}{L}(\varepsilon_n - \varepsilon_{n-1}) = 0 \tag{8}$$

where m is the mass of the corresponding section, $\tan\delta$ is the effective loss factor of the lattice, which equals the loss modulus divided by the storage modulus, A is the cross-sectional area of the lattice, L is the distance interval between two adjacent pairs of electrodes, ε_{n-1} is the strain of the $(n-1)$th pair of electrodes ($n = 2, 3, 4$) and ε_n is the strain transmitted to the nth pair of electrodes.

Solving this equation yields the ratio of transient displacement transmissibility $\left(\frac{\epsilon_n}{\epsilon_{n-1}}\right)$ between each adjacent pairs of electrodes:

$$\frac{\epsilon_n}{\epsilon_{n-1}} = \left[\frac{1 + (r\tan\delta)^2}{(1 - r^2)^2 + (r\tan\delta)^2}\right]^{\frac{1}{2}} \tag{9}$$

where r is the frequency ratio and can be derived from[37]

$$r = \frac{8\pi C_{\text{p}}}{\lambda}\sqrt{\frac{mL}{E_{\text{eff}} A}} \tag{10}$$

where λ is the wavelength, C_p is the propagation speed of the elastic wave induced by the impact and can be calculated by dividing the distance between adjacent pairs of electrodes by the corresponding time interval. The distance between the wavefront and peak strain position is 1/4 of the wavelength (Fig. 4e). Combining equations (7) and (9) results in equation (6) and

$$\frac{V_n^{\text{p}}}{V_{n-1}^{\text{p}}} = \left[\frac{1 + (r\tan\delta)^2}{(1 - r^2)^2 + (r\tan\delta)^2}\right]^{\frac{1}{2}} \tag{11}$$

which relates the voltage from each pair of patterned electrodes with the loss modulus of the material between the electrodes. V_n^p is the peak value of the voltage output of the nth pair of electrodes. The fitted straight line of the semilogarithmic relationship in Fig. 4f validates and matches well the uniform damping coefficient within each section of the microlattice employed here.

Patterned capacitors. The capacitance of each electrode pair embedded within the flexible rod is related to the gap distance between its neighbouring electrodes and changes once compression or tension is applied:

$$C = \frac{\varepsilon A_{\text{c}}}{t} \tag{12}$$

where A_c is the surface area of the electrodes, which is a constant in our design (1 mm^2), ε is the permittivity of the flexible dielectric composite and t is the space between the paired electrodes.

Data availability

The data that support the plots within this paper and other findings of this study are available from the corresponding author upon reasonable request.

Received: 7 July 2019; Accepted: 28 February 2020;
Published online: 6 April 2020

References

1. Madou, M. J. *Fundamentals of Microfabrication: The Science of Miniaturization* 2nd edn (CRC Press, 2002).
2. Liu, N. et al. Three-dimensional photonic metamaterials at optical frequencies. *Nat. Mater.* **7**, 31–37 (2008).
3. Radke, A., Gissibl, T., Klotzbücher, T., Braun, P. V. & Giessen, H. Three-dimensional bichiral plasmonic crystals fabricated by direct laser writing and electroless silver plating. *Adv. Mater.* **23**, 3018–3021 (2011).
4. Macdonald, E. et al. 3D printing for the rapid prototyping of structural electronics. *IEEE Access* **2**, 234–242 (2014).
5. Yan, Z. et al. Mechanical assembly of complex, 3D mesostructures from releasable multilayers of advanced materials. *Sci. Adv.* **2**, e1601014 (2016).
6. Xu, S. et al. Assembly of micro/nanomaterials into complex, three-dimensional architectures by compressive buckling. *Science* **347**, 154–159 (2015).
7. Sun, Y., Choi, W. M., Jiang, H., Huang, Y. Y. & Rogers, J. A. Controlled buckling of semiconductor nanoribbons for stretchable electronics. *Nat. Nanotechnol.* **1**, 201–207 (2006).
8. Adams, J. J. et al. Conformal printing of electrically small antennas on three-dimensional surfaces. *Adv. Mater.* **23**, 1335–1340 (2011).
9. Saleh, M. S., Hu, C. & Panat, R. Three-dimensional microarchitected materials and devices using nanoparticle assembly by pointwise spatial printing. *Sci. Adv.* **3**, e1601986 (2017).
10. Kim, Y., Yuk, H., Zhao, R., Chester, S. A. & Zhao, X. Printing ferromagnetic domains for untethered fast-transforming soft materials. *Nature* **558**, 274–279 (2018).
11. Cui, H. et al. Three-dimensional printing of piezoelectric materials with designed anisotropy and directional response. *Nat. Mater.* **18**, 234–241 (2019).
12. Huang, Y. et al. Assembly and applications of 3D conformal electronics on curvilinear surfaces. *Mater. Horiz.* **6**, 642–683 (2019).
13. MacDonald, E. & Wicker, R. Multiprocess 3D printing for increasing component functionality. *Science* **353**, aaf2093 (2016).

14. Wu, S.-Y., Yang, C., Hsu, W. & Lin, L. 3D-printed microelectronics for integrated circuitry and passive wireless sensors. *Microsyst. Nanoeng.* **1**, 15013 (2015).
15. Lin, R., Li, Y., Mao, X., Zhou, W. & Liu, R. Hybrid 3D printing all-in-one heterogenous rigidity assemblies for soft electronics. *Adv. Mater. Technol.* **4**, 1900614 (2019).
16. Suntivich, R., Shchepelina, O., Choi, I. & Tsukruk, V. V. Inkjet-assisted layer-by-layer printing of encapsulated arrays. *ACS Appl. Mater. Interfaces* **4**, 3102–3110 (2012).
17. Oran, D. et al. 3D nanofabrication by volumetric deposition and controlled shrinkage of patterned scaffolds. *Science* **362**, 1281–1285 (2018).
18. Oh, Y.-J., Cho, S. M. & Chung, C.-H. An in situ ATR-FTIR study on palladium displacement reaction on hydrogen-terminated silicon surface. *J. Electrochem. Soc.* **152**, C348–C355 (2005).
19. Abrantes, L. M. & Correia, J. P. On the mechanism of electroless Ni–P plating. *J. Electrochem. Soc.* **141**, 2356–2360 (1994).
20. Matula, R. A. Electrical resistivity of copper, gold, palladium and silver. *J. Phys. Chem. Ref. Data* **8**, 1147–1298 (1979).
21. Gao, Y. et al. 3D-printed coaxial fibers for integrated wearable sensor skin. *Adv. Mater. Technol.* **4**, 1900504 (2019).
22. Ladd, C., So, J.-H., Muth, J. & Dickey, M. D. 3D printing of free standing liquid metal microstructures. *Adv. Mater.* **25**, 5081–5085 (2013).
23. Seifert, T. et al. Additive manufacturing technologies compared: morphology of deposits of silver ink using inkjet and aerosol jet printing. *Ind. Eng. Chem. Res.* **54**, 769–779 (2015).
24. Nakanishi, T., Masuda, Y. & Koumoto, K. Site-selective deposition of magnetite particulate thin films on patterned self-assembled monolayers. *Chem. Mater.* **16**, 3484–3488 (2004).
25. Ichinose, I., Senzu, H. & Kunitake, T. A surface sol–gel process of TiO_2 and other metal oxide films with molecular precision. *Chem. Mater.* **9**, 1296–1298 (1997).
26. Saito, N. et al. Low-temperature fabrication of light-emitting zinc oxide micropatterns using self-assembled monolayers. *Adv. Mater.* **14**, 418–421 (2002).
27. Tian, D. et al. A Pd-free activation method for electroless nickel deposition on copper. *Surf. Coat. Technol.* **228**, 27–33 (2013).
28. *Periodic Table and X-ray Energies* (accessed 2018); https://www.bruker.com/fileadmin/user_upload/8-PDF-Docs/X-rayDiffraction_ElementalAnalysis/HH-XRF/Misc/Periodic_Table_and_X-ray_Energies.pdf
29. Jiang, L., Gao, L. & Sun, J. Production of aqueous colloidal dispersions of carbon nanotubes. *J. Colloid Interface Sci.* **260**, 89–94 (2003).
30. Kim, D.-H. et al. Epidermal electronics. *Science* **333**, 838–843 (2011).
31. Yeom, C. et al. Large-area compliant tactile sensors using printed carbon nanotube active-matrix backplanes. *Adv. Mater.* **27**, 1561–1566 (2015).
32. Wang, X. et al. Recent progress in electronic skin. *Adv. Sci.* **2**, 1500169 (2015).
33. Meerbeek, I. M. V., Sa, C. M. D. & Shepherd, R. F. Soft optoelectronic sensory foams with proprioception. *Sci. Robot.* **3**, eaau2489 (2018).
34. Yao, D. et al. Achieving the upper bound of piezoelectric response in tunable, wearable 3D printed nanocomposites. *Adv. Funct. Mater.* **29**, 1903866 (2019).
35. Dressick, W. J., Dulcey, C. S., Georger, J. H., Calabrese, G. S. & Calvert, J. M. Covalent binding of Pd catalysts to ligating self-assembled monolayer films for selective electroless metal deposition. *J. Electrochem. Soc.* **141**, 210–220 (1994).
36. Chen, D. & Zheng, X. Multi-material additive manufacturing of metamaterials with giant, tailorable negative Poisson's ratios. *Sci. Rep.* **8**, 9139 (2018).
37. Inman, D. J. & Singh, R. C. *Engineering Vibration* Vol. 3 (Prentice Hall, 1994).

Acknowledgements

We acknowledge NSF_CMMI 1727492, DARPA Young Faculty Award (D20AP00001, Program Manager, R. Rolcawich), Air Force Office of Scientific Research (AFOSR) (FA9550-18-1-0299), and Office of Naval Research (N00014-19-1-2723:P00001) for financial support of this work. We would like to acknowledge the help of H.C. Liu for the antenna array collaboration.

Author contributions

X.Z. and R.H. conceived and designed the research. R.H. formulated charged resin materials, performed depositions, synthesized the functionalized piezoelectric materials and took SEM and optical images. H.C. designed and fabricated samples, performed device testing, derived wave propagation equations and took SEM images. Z.X. fabricated the multi-material samples and assisted with testing. D.Y. derived elastic wave propagation within the piezoelectric materials. J.M. and J.B. designed antenna structures. All authors participated in drafting the manuscript, discussion and interpretation of the data.

Competing interests

A worldwide patent application related to this work has been filed (no. PCT/US2019/033385). The authors declare no other competing interests.

Additional information

Supplementary information is available for this paper at https://doi.org/10.1038/s41928-020-0391-2.

Correspondence and requests for materials should be addressed to X.Z.

Reprints and permissions information is available at www.nature.com/reprints.

Publisher's note Springer Nature remains neutral with regard to jurisdictional claims in published maps and institutional affiliations.

Terms and Conditions

Springer Nature journal content, brought to you courtesy of Springer Nature Customer Service Center GmbH (“Springer Nature”).
Springer Nature supports a reasonable amount of sharing of research papers by authors, subscribers and authorised users (“Users”), for small-scale personal, non-commercial use provided that all copyright, trade and service marks and other proprietary notices are maintained. By accessing, sharing, receiving or otherwise using the Springer Nature journal content you agree to these terms of use (“Terms”). For these purposes, Springer Nature considers academic use (by researchers and students) to be non-commercial.
These Terms are supplementary and will apply in addition to any applicable website terms and conditions, a relevant site licence or a personal subscription. These Terms will prevail over any conflict or ambiguity with regards to the relevant terms, a site licence or a personal subscription (to the extent of the conflict or ambiguity only). For Creative Commons-licensed articles, the terms of the Creative Commons license used will apply.
We collect and use personal data to provide access to the Springer Nature journal content. We may also use these personal data internally within ResearchGate and Springer Nature and as agreed share it, in an anonymised way, for purposes of tracking, analysis and reporting. We will not otherwise disclose your personal data outside the ResearchGate or the Springer Nature group of companies unless we have your permission as detailed in the Privacy Policy.
While Users may use the Springer Nature journal content for small scale, personal non-commercial use, it is important to note that Users may not:

1. use such content for the purpose of providing other users with access on a regular or large scale basis or as a means to circumvent access control;
2. use such content where to do so would be considered a criminal or statutory offence in any jurisdiction, or gives rise to civil liability, or is otherwise unlawful;
3. falsely or misleadingly imply or suggest endorsement, approval , sponsorship, or association unless explicitly agreed to by Springer Nature in writing;
4. use bots or other automated methods to access the content or redirect messages
5. override any security feature or exclusionary protocol; or
6. share the content in order to create substitute for Springer Nature products or services or a systematic database of Springer Nature journal content.

In line with the restriction against commercial use, Springer Nature does not permit the creation of a product or service that creates revenue, royalties, rent or income from our content or its inclusion as part of a paid for service or for other commercial gain. Springer Nature journal content cannot be used for inter-library loans and librarians may not upload Springer Nature journal content on a large scale into their, or any other, institutional repository.
These terms of use are reviewed regularly and may be amended at any time. Springer Nature is not obligated to publish any information or content on this website and may remove it or features or functionality at our sole discretion, at any time with or without notice. Springer Nature may revoke this licence to you at any time and remove access to any copies of the Springer Nature journal content which have been saved.
To the fullest extent permitted by law, Springer Nature makes no warranties, representations or guarantees to Users, either express or implied with respect to the Springer nature journal content and all parties disclaim and waive any implied warranties or warranties imposed by law, including merchantability or fitness for any particular purpose.
Please note that these rights do not automatically extend to content, data or other material published by Springer Nature that may be licensed from third parties.
If you would like to use or distribute our Springer Nature journal content to a wider audience or on a regular basis or in any other manner not expressly permitted by these Terms, please contact Springer Nature at

onlineservice@springernature.com